Muonium in diamond

E. Holzschuh, W. Kündig, P. F. Meier, and B. D. Patterson
Physik-Institut, Universität Zürich, 8001 Zürich, Switzerland

J. P. F. Sellschop and M. C. Stemmet
Nuclear Physics Research Unit, University of the Witwatersrand, Johannesburg 2001, South Africa

H. Appel
Kernforschungszentrum Karlsruhe und Universität Karlsruhe, 7500 Karlsruhe, Germany
(Received 9 September 1981)

Two muonium states have been found in diamond. "Normal" muonium shows an isotropic hyperfine interaction with a coupling constant $A/h = 3711 \pm 21$ MHz. "Anomalous" muonium is described by a $\langle 111 \rangle$ axially symmetric spin Hamiltonian with coupling constants extrapolated to 0 K $|A_{\parallel}|/h = 167.98 \pm 0.06$ MHz and $|A_{\perp}|/h = 392.59 \pm 0.06$ MHz. $A_{\parallel}$ and $A_{\perp}$ are of opposite sign, and they exhibit a temperature dependence describable by a Debye model. The amplitudes of the three anomalous muonium hyperfine transitions in zero applied field increase with increasing temperature and show relative variations which give information about muonium formation and indicate that anomalous muonium is the most stable state for muons in diamond. These diamond results are compared with those from the isostructural materials silicon and germanium.

I. INTRODUCTION

A positive muon stopped in an insulator or semiconductor may bind an electron to form muonium ($\mu^+ e^- = \mathrm{Mu}$). Since the muon mass is much larger than the electron mass, muonium can be considered a light isotope of hydrogen, and Mu and H have similar properties in vacuum (see Table I). It is expected that these two atoms when implanted in a solid also have similar electronic structures.

Two different muonium states named normal muonium Mu and anomalous muonium Mu* have been detected in Si (Refs. 1 and 2) as well as in Ge.[3] In an extension of this research, we have investigated diamond and have again found the corresponding states. Our measurements were performed on a powder sample and on a single crystal as a function of temperature and applied magnetic field.

The formation of a paramagnetic muon state can be observed via the characteristic precession pattern of the muon spin polarization under the influence of the bound electron and the applied field. In a muon-spin-rotation (μSR) experiment,[4] polarized positive muons are stopped in the material to be investigated, and the positrons from the muon decay ($\tau_{\mu} = 2.2$ μs) are recorded as a function of the time after a muon stop. Since positron emission is most probable in the direction of the muon

TABLE I. Comparison of hydrogen and muonium.

	H	Mu
Mass (m_e)	1837.15	207.769
Reduced electron mass (m_e)	0.999 456	0.995 187
Ground-state radius a (Å)	0.529 465	0.531 736
Ground-state energy (eV)	−13.5984	−13.5403
Nuclear gyromagnetic ratio γ ($s^{-1}T^{-1}$)	$2.675\,20 \times 10^8$	$8.516\,07 \times 10^8$
Hyperfine frequency ν_0 (GHz)	1.420 41	4.463 30

spin, the counting rate is modulated with the muon precession frequencies. This type of measurement requires that not more than one muon be present in the sample at any one time.

The Hamiltonian which determines the time evolution of the muon spin in normal muonium has the form of that for vacuum muonium:

$$H_{\mathrm{Mu}}=A\vec{\mathrm{I}}\cdot\vec{\mathrm{S}}-g_e\mu_B^e\vec{\mathrm{S}}\cdot\vec{\mathrm{B}}-g_\mu\mu_B^\mu\vec{\mathrm{I}}\cdot\vec{\mathrm{B}}\ , \tag{1}$$

where $\vec{\mathrm{I}}$ and $\vec{\mathrm{S}}$ are the spin operators of the muon and the electron, respectively. The vacuum values of the g factors and magnetic moments are given in Sec. II. For the $1s$ state, the hyperfine constant A is proportional to the electron density at the muon site

$$A=h\nu_0=-\tfrac{2}{3}\mu_0 g_\mu g_e\mu_B^\mu\mu_B^e\,|\,\psi(0)\,|^2\ . \tag{2}$$

The values of A for Si and Ge are considerably reduced compared to the vacuum values

$$A(\mathrm{Si})/A(\mathrm{vac})=0.44$$

and

$$A(\mathrm{Ge})/A(\mathrm{vac})=0.53\ .$$

The diamond result is given in Sec. IV A. Mu can probably be considered a "deep" impurity in Si and Ge, the theory of which is difficult and incomplete. Various models for Mu in Si and Ge which treat the reduced A values have been reported, and in Sec. V these models are reexamined in light of the diamond data.

Anomalous muonium in Si and Ge can be described by a Hamiltonian whose hyperfine interaction has axial symmetry about one of the four equivalent $\langle 111\rangle$ directions z:

$$H_{\mathrm{Mu}^*}=A_\perp(I_xS_x+I_yS_y)+A_{||}I_zS_z-g_e\mu_B^e\vec{\mathrm{S}}\cdot\vec{\mathrm{B}}-g_\mu\mu_B^\mu\vec{\mathrm{I}}\cdot\vec{\mathrm{B}}\ . \tag{3}$$

The Mu* hyperfine parameters are much smaller than the vacuum Mu value

$$A_\perp(\mathrm{Si})/A(\mathrm{vac})=0.020\ ,$$

$$A_\perp(\mathrm{Ge})/A(\mathrm{vac})=0.029\ ,$$

$$A_{||}/A_\perp=0.20\ .$$

These small values and the large anisotropy indicate that Mu* is very different from vacuum muonium, and no satisfactory model of its electronic structure has been reported so far. The measurements on single crystal diamond presented in Sec. IV B show that H_{Mu^*} also applies for diamond, with the same symmetry axis.

The temperature dependence of $A_\perp$ and $A_{||}$ in Si was first reported by Blazey *et al.*,[5] and our measurements on diamond described in Sec. IV C give a similar result. In these measurements a large and nonmonotonic variation of the precession amplitudes was observed at high temperature. A model is presented in Sec. IV E which attributes this variation to thermally activated transitions among the various muon states.

A "magic"-field method is described in Sec. II B which allows powder measurements on Mu* in an external field. This method makes possible the study of the Mu* hyperfine parameters without an expensive single crystal.

II. ENERGY LEVELS OF MUONIUM

A. Normal muonium (Mu)

The eigenvalues of the spin Hamiltonian H_{Mu} [Eq. (1)] for normal muonium are

$$\begin{aligned}E_{1,3}&=A/4\pm h\nu_-B\ ,\\ E_{2,4}&=-A/4\pm[A^2/4+(h\nu_+B)^2]^{1/2}\ ,\end{aligned} \tag{4}$$

where

$$\nu_\pm=(-g_e\mu_B^e\pm g_\mu\mu_B^\mu)/(2h)\ .$$

For vacuum muonium the constants are

$$\begin{aligned}g_e&=g_{e'}(1-\tfrac{1}{3}\alpha^2)=-2(1.001\,1419)\ ,\\ g_\mu&=g_{\mu'}(1-\tfrac{1}{3}\alpha^2)=+2(1.001\,1481)\ ,\\ \mu_B^e&=e\hbar/(2m_e)=9.274\,08\times10^{-24}\ \mathrm{J\,T^{-1}}\ ,\\ \mu_B^\mu&=e\hbar/(2m_\mu)=4.485\,24\times10^{-26}\ \mathrm{J\,T^{-1}}\ ,\end{aligned} \tag{5}$$

where $g_{e'}$ and $g_{\mu'}$ are the free-particle g factors, g_e and g_μ are the bound g factors, and α is the fine-structure constant. The numerical values for $\nu_\pm$ are

$$\begin{aligned}\nu_+&=14.079\,87\ \mathrm{GHz/T}\ ,\\ \nu_-&=13.944\,34\ \mathrm{GHz/T}\ .\end{aligned} \tag{6}$$

The energy-level diagram for normal muonium is shown in Fig. 1. In an external magnetic field transverse to the initial polarization $P_x(0)$, the indicated $\Delta m=\pm1$ transitions can be observed.

The time-dependent polarization of the muon is then

$$P_x(t)=\tfrac{1}{4}[(1+k)\cos(\omega_{12}t)+(1-k)\cos(\omega_{23}t)+(1-k)\cos(\omega_{14}t)+(1+k)\cos(\omega_{34}t)]P_x(0) \tag{7}$$

with

$$k=\nu_+ B/[\nu_0^2/4+(\nu_+ B)^2]^{1/2}$$

and

$$\omega_{ij}=2\pi\nu_{ij}=(E_i-E_j)/\hbar\ .$$

Owing to the limited time resolution of the particle detectors in this experiment, only the transition frequencies ν_{12} and ν_{23} in the low-field Zeeman region are observed. A direct observation of the hyperfine frequency ν_0 in zero external field has recently been performed in Si, Ge, and SiO_2 with a μSR apparatus of high time resolution.[6]

B. Anomalous muonium (Mu*)

The eigenvalues of the spin Hamiltonian H_{Mu^*} for anomalous muonium [Eq. (3)] depend on the angle θ between the symmetry axis and $\vec{B}$. Exact analytical solutions can be found for $\theta=0$ and $\pi/2$ by diagonalizing H_{Mu^*}:

$$\begin{aligned}
&E_{1,3}(\theta=0)=A_{||}/4\pm h\nu_- B\ ,\\
&E_{2,4}(\theta=0)=-A_{||}/4\pm[A_\perp^2/4+(h\nu_+ B)^2]^{1/2}\ ,\\
&E_{1,3}(\theta=\pi/2)=A_\perp/4\pm[(A_{||}-A_\perp)^2/16+(h\nu_- B)^2]^{1/2}\ ,\\
&E_{2,4}(\theta=\pi/2)=-A_\perp/4\pm[(A_{||}+A_\perp)^2/16+(h\nu_+ B)^2]^{1/2}\ .
\end{aligned} \tag{8}$$

The indices are chosen in such a way that for $A_{||}=A_\perp=A$, Eqs. (8) transform into Eqs. (4). As an illustration, Fig. 2 gives the energy-level diagram for Mu* in diamond using the hyperfine constants determined in the experimental part of this article. At high fields only the transitions ν_{12} and ν_{34} can be detected, since the amplitudes for the others are practically zero.

Approximate expressions for the transition frequencies ν_{12} and ν_{34} at fields $B>>(A_\perp,A_{||})/\mu_B^e$ can be obtained[7] for arbitrary angles θ:

$$\nu_{12,34}\simeq\{\ [\nu_\mu\mp\tfrac{1}{2}(A_\perp\sin^2\theta+A_{||}\cos^2\theta)/h]^2 +[\tfrac{1}{4}(A_{||}-A_\perp)\sin(2\theta)/h]^2\ \}^{1/2}\ , \tag{9}$$

where

$$\nu_\mu=\nu_L B=0.135\,537B\ \mathrm{GHz/T} \tag{10}$$

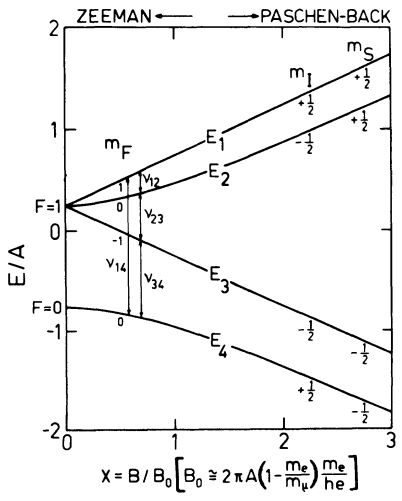

FIG. 1. Breit-Rabi diagram for normal muonium. The magnetic field X is measured in units of B_0. In vacuum, $B_0(\mathrm{vac})=0.158\,68$ T. The transitions indicated correspond to the observable μSR frequencies in a transverse field.

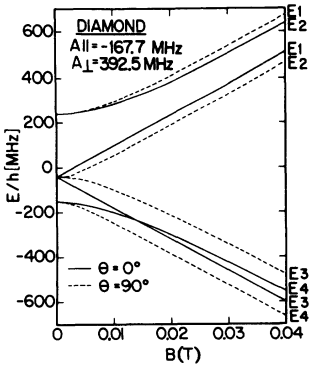

FIG. 2. Energy-level diagram for anomalous muonium in diamond for $\theta=0°$ and 90°.

is the Larmor frequency of the free muon. It is interesting to note that for

$$B=B_M=(A_\perp+A_{||})/(4h\nu_L)\ ,$$

Eq. (9) implies that

$$\nu_{12}=\nu_M\simeq\tfrac{1}{4}(A_\perp-A_{||})/h$$

is independent of the crystal orientation θ. As will be shown in Sec. IV D this allows the observation of a Mu* signal at the magic field B_M in a powder sample.

More accurate expressions for B_M and ν_M can be obtained from Eq. (8) by setting

$$\nu_{12}(\theta=0)=\nu_{12}(\theta=\pi/2)\ .$$

The result, to order $(m_e/m_\mu)^2$, is

$$\begin{aligned}
B_M&=\frac{1}{4h\nu_L}\left[A_\perp+A_{||}-2A_\perp\left[\frac{m_e}{m_\mu}\right]+\frac{A_{||}(2A_\perp+A_{||})}{(A_\perp+A_{||})}\left[\frac{m_e}{m_\mu}\right]^2+\cdots\right]\ ,\\
\nu_M&=\frac{1}{4h}\left[A_\perp-A_{||}+\frac{2A_\perp(A_\perp-A_{||})}{(A_\perp+A_{||})}\left[\frac{m_e}{m_\mu}\right]+\frac{4A_\perp^3-2A_\perp^2A_{||}+3A_\perp A_{||}^2+A_{||}^3}{(A_\perp+A_{||})^2}\left[\frac{m_e}{m_\mu}\right]^2+\cdots\right]\ .
\end{aligned}\tag{11}$$

If ν_M and B_M are known, the hyperfine coupling constants may be determined by

$$\frac{A_{||}}{h}=2(B_M\nu_L-\nu_M)+2\frac{(B_M\nu_L+\nu_M)^2}{B_M\nu_L}\left[\frac{m_e}{m_\mu}\right]+2\frac{B_M^3\nu_L^3-3\nu_M^2B_M\nu_L-2\nu_M^3}{B_M^2\nu_L^2}\left[\frac{m_e}{m_\mu}\right]^2+\cdots\ ,$$

$$\frac{A_\perp}{h}=2(B_M\nu_L+\nu_M)+2\frac{B_M^2\nu_L^2-\nu_M^2}{B_M\nu_L}\left[\frac{m_e}{m_\mu}\right]+\frac{6\nu_M^3+\nu_M^2B_M\nu_L+2\nu_MB_M^2\nu_L^2-B_M^3\nu_L^3}{B_M^2\nu_L^2}\left[\frac{m_e}{m_\mu}\right]^2+\cdots\ .\tag{12}$$

From the high-field approximation[7] for $\vec{P}_\mu(t)$, it can be shown that at B_M a fraction $\frac{11}{30}$ of the μ^+ polarization in Mu* oscillates with ν_M, $\frac{4}{30}$ are time independent, and $\frac{15}{30}$ remain unobservable.

In zero field, three Mu* frequencies can be observed. These are given by [Eq. (8)]

$$\begin{aligned}
\nu_1&=(A_\perp+A_{||})/2h\ ,\\
\nu_2&=(A_\perp-A_{||})/2h\ ,\\
\nu_3&=A_\perp/h\ ,
\end{aligned}\tag{13}$$

and satisfy the relation $\nu_1+\nu_2=\nu_3$.

The case of zero field was also treated in Ref. 7, and the polarization $P_x(t)$ averaged over all crystal orientations (i.e., for a powder sample) is given by

$$P_x(t)=\tfrac{1}{6}[1+2\cos(\omega_1t)+2\cos(\omega_2t)+\cos(\omega_3t)]P_x(0)\ .\tag{14}$$

III. EXPERIMENTAL DETAILS

The measurements reported were performed on a powder sample and on a single crystal. The powder sample consisted of 10 g of type-IIa diamond with a grain size of $1-6$ μm. Type-IIa diamond is characterized as the purest diamond found in nature.

The single crystal sample was the "Maltese cross" diamond, a 46-ct (9.2-g) diamond of type Ia. Ia diamonds contain on the order of 0.1 at.% nitrogen and are therefore slightly yellow. The crystal is a cube with 14-mm edges parallel to the $\langle 100\rangle$ directions. This large diamond contains what is believed to be an aggregation of inclusions which appear optically as a beautiful three-dimensional Maltese cross.

The experiments were performed at the Swiss Institute for Nuclear Research (SIN), where intense beams of polarized positive muons from the superconducting muon channels are available. A μSR setup with either two or four positron counters was used. The time resolution of $1.0-1.2$-ns full width at half maximum (FWHM) allowed the observation of frequencies up to approximately 500 MHz. Magnetic fields up to 0.5 T could be generated by Helmholtz coils, and the earth field could be compensated by three pairs of "zero-field" coils. For the zero-field measurements of anomalous muonium in the powder sample, the residual field at the sample was smaller than 2 μT. A more detailed description of our apparatus is found in Ref. 4.

A He-bath cryostat was used for the single-crystal measurements at 4.2 K. The temperature

of the powder sample was controlled by a He-flow cryostat below room temperature (RT), and above RT a high-vacuum hot finger oven was used. The ratio of muon stops in the sample to muon stops in the cryostat or oven material was measured by removing the target from the beam and was in the range 3.5:1 to 4.5:1. The signal amplitudes quoted in this article have been corrected by this ratio.

The general form of a μSR spectrum consists of an exponential decay which is modulated by a sum of damped sinusoidal oscillations corresponding to the time-dependent muon polarization

$$N(t)=N_0 e^{-t/\tau_\mu}[1+X(t)]+b \ , \tag{15a}$$

$$X(t)=\sum_{j=1}^{n} a_j R_j(t)\cos(2\pi\nu_j t+\phi_j) \ . \tag{15b}$$

N_0 is a normalization constant and b is a background assumed to be constant. The a_j, ν_j, and ϕ_j are the amplitudes, precession frequencies, and initial phase angles of the n different contributions to the muon polarization. In the data analysis, the damping functions were assumed to have the form

$$R_j(t)=\exp(-\lambda_j t) \ .$$

To determine the number n of significant signals and the approximate frequencies, the modulation spectra $X(t)$ were Fourier transformed. Then, least-square fits of the data to Eq. (15) were performed. A single damping rate λ was assumed for all the signals corresponding to a particular muonium state. Some of the single-crystal spectra showed a large number of weak signals. In these cases least-square fits of the complex Fourier spectra to the Fourier transform of Eq. (15b) were performed. A comparison showed that the two methods yielded identical results.

In each run, $(2-3)\times 10^7$ good events were accumulated, corresponding to a counting time of 2 to 3 h and resulting in a typical statistical accuracy of the frequencies of the observed signals in the range 0.1 to 0.01 MHz.

IV. EXPERIMENTAL RESULTS

A. Normal muonium

Mu was observed in the powder sample in the low-field Zeeman region. Measurements were performed in fields from 1 to 20 mT, and signals could be observed at temperatures from 4.2 to 150 K (Fig. 3). The two lines seen in the frequency spectrum are the transitions ν_{12} and ν_{23} indicated

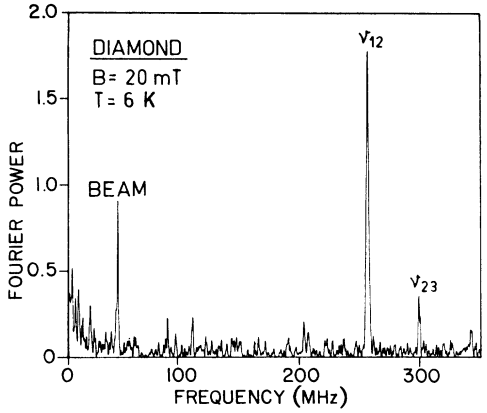

FIG. 3. μSR spectrum of normal muonium in diamond powder at 6 K in a field of 20 mT. The observed frequencies ν_{12} and ν_{23} are indicated in Fig. 1.

in the Breit-Rabi diagram (Fig. 1). The third line at 50.63 MHz is a background signal at the cyclotron frequency of the SIN accelerator. From the formulas in Eq. (4), an expression for the hyperfine frequency ν_0 can be derived which contains only experimentally measured quantities:

$$\nu_0=A/h=\tfrac{1}{2}[(\nu_{12}+\nu_{23}+2\nu_\mu)^2/\Delta\nu-\Delta\nu] \ , \tag{16}$$

where

$$\Delta\nu=\nu_{23}-\nu_{12} \ ,$$

and ν_μ is the free-muon-precession frequency [Eq. (10)]. Under the assumption that the muonic g factor g_μ is not appreciably influenced by the solid host, we obtain in addition the electronic g factor g_e,

$$g_e=-\frac{m_e}{m_\mu}g_\mu[(\nu_{12}+\nu_{23})/\nu_\mu+1] \ . \tag{17}$$

The results from the measurements at 6 K are

$$\begin{aligned} A/h &= 3711\pm 21 \text{ MHz} \ , \\ g_e &= -2.0034\pm 0.0017 \ . \end{aligned} \tag{18}$$

The hyperfine coupling constant corresponds to $83.2\pm 0.5\%$ of the vacuum value (see Table I) or a 6.3% increase over the vacuum radius a_{Mu}.

The amplitude and relaxation rate of the Mu signal was studied as a function of temperature at a field of 0.975 ± 0.015 mT. At this field the frequencies ν_{12} and ν_{23} are approximately equal

$$(\nu_{12}\cong\nu_{23}\cong\nu_{-}B=13.6 \text{ MHz})$$

and were not resolved. The result of the fits, assuming $R(t)=\exp(-\lambda t)$, are listed in Table II.

TABLE II. Experimentally determined asymmetry and relaxation rates for normal muonium in powdered diamond. The measurements were performed at 0.975 mT.

T (K)	a (%)	λ (μs^{-1})
8.1	1.75±0.20	1.95±0.27
22.7	1.30±0.18	1.78±0.30
42	1.52±0.17	1.77±0.26
66.5	1.84±0.20	2.85±0.42
87	1.35±0.15	2.38±0.37
105	1.29±0.15	2.33±0.37
123	1.20±0.25	3.02±0.78
150	2.0 ±0.5	4.6 ±1.6

Within errors, the amplitude is temperature independent, whereas λ increases with increasing temperature such that above 150 K no Mu signal could be detected. For measurements of $\sim 2\times 10^7$ decay positrons, the upper limit for a detectable Mu signal is $\lambda = 5-10\ \mu s^{-1}$. The asymmetries were normalized by a measurement of the effective asymmetry for a Cu sample ($a_{\text{eff}} \cong 0.20$) to give the formation probability of Mu in diamond. The result is given in Table III. It is worthwhile to note that the Mu signals in Ge (Si) vanish at about 100 K (300 K) also due to strong relaxation effects.

B. Hyperfine parameters of Mu*

In order to unambiguously determine the symmetry and the parameters of the hyperfine interaction of Mu*, measurements on a single crystal are required. The field dependence of the μSR frequencies was measured at 4.2 K with the ⟨110⟩ axis parallel to the applied field. In this orientation two of the ⟨111⟩ axes are at $\theta = 90°$ and two ⟨111⟩ axes at $\theta = 35.26°$ with respect to the external field. The observed frequencies for the ⟨110⟩ orientation are shown in Fig. 4. Additional measurements were made with the field parallel to the ⟨100⟩ direction (Fig. 5). For this orientation all four body diagonals make an angle $\theta = 54.74°$ with the field. At all nonzero applied fields, the only Mu* signals observed were ν_{12} and ν_{34} (see Fig. 2). These two frequencies critically depend on the angle θ, and a misalignment of the crystal by $\cong 0.2°$ for $\theta = 35.26°$ (54.74°) already makes the observation of the lines difficult. A misalignment is the reason for the limited number of data points for $\theta = 35.26°$. The effect of a deviation $\Delta\theta$ from $\theta = 90°$ is much smaller, because at that angle the frequencies only depend on $\Delta\theta^2$.

The experimental points are well represented by the spin Hamiltonian given by Eq. (3). The μSR frequencies $\nu_{12}(B)$ and $\nu_{34}(B)$ from the $\theta = 90°$ data (Fig. 4) were fitted to Eq. (8) resulting in $\chi^2 = 33$ for 19 degrees of freedom. The best estimates for the hyperfine parameters are

$$
\begin{aligned}
&|A_\perp|/h = 392.52\pm 0.07\ \text{MHz}\ , \\
&|A_{||}|/h = 167.72\pm 0.23\ \text{MHz}\ , \\
&A_\perp/A_{||} < 0\ , \\
&g_e = -1.9932\pm 0.0043\ , \\
&g_\mu = +2.0016\pm 0.0017\ .
\end{aligned}
\tag{19}
$$

As already noted, a crystal misalignment has more serious consequences for the $\theta = 35°$ frequencies than for those with $\theta = 90°$. The observed position and splitting of the 35° lines was used to estimate the true orientation of the crystal. The deviation from $\theta = 90°$ was $\Delta\theta = 1.0° \pm 0.5°$. The effect of this deviation was investigated by fitting simulated data to Eq. (8) and was found to be 150 (440) ppm for $A_\perp$, $A_{||}$ (g_e,g_μ). The values above include a correction to account for this deviation, and the quoted errors are the sums of the statistical standard deviations and the corrections. The lines drawn through the data points for $\theta = 35.26°$ (Fig. 4) and $\theta = 54.74°$ (Fig. 5) were calculated from the values given in Eq. (19). Figure 6 shows the measured θ dependence of the Mu* frequencies ν_{12} and ν_{34} obtained at a field of 0.2 T and clearly indicates that

TABLE III. Formation probabilities for muon states in diamond. The values are corrected for background from cryostat, etc., and normalized with the precession amplitude in a Cu sample.

	T (K)	Mu (%)	Mu* (%)	μ^+ (%)	Missing (%)
Powder	4.2–90	18.5±0.9	9.9±0.7	<10	≳60
Powder, magic field	296		14.5±1.3	<5	≳80
Single crystal	4.2	20 ±4	11.9±0.9	<10	≳60

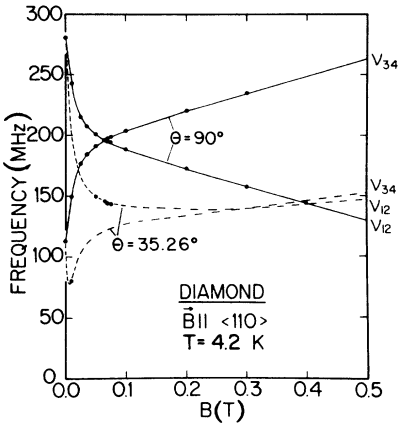

FIG. 4. Mu* frequencies as a function of the applied field for single-crystal diamond with $\vec{B}||\langle 110\rangle$. At this orientation, two $\langle 111\rangle$ axes are at $\theta=90°$ and two $\langle 111\rangle$ at $\theta=35.26°$ with respect to $\vec{B}$. Alignment errors cause a splitting of the $\theta=35.26°$ signals, making their detection difficult. Curves are calculated with the parameters from Eq. (19).

Mu* has $\langle 111\rangle$ symmetry.

It is noteworthy that $A_{||}$ and $A_{\perp}$ have opposite signs, in contrast to the case of Si and Ge, implying an even stronger anisotropy. We cannot discount the possibility that g_e is anisotropic. Since the analysis above was performed for $\theta=90°$, "g_e" would then be "$g_{\perp}$". For an estimate of an upper limit of an anisotropy in g_e, we refer to Sec. IV D.

The measurements on the single crystal at low fields also exhibit normal muonium signals. The

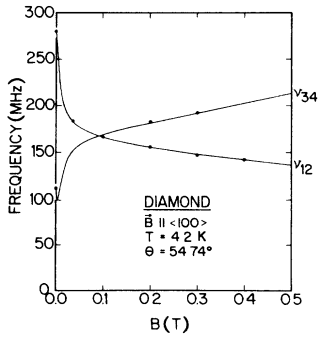

FIG. 5. Mu* frequencies as a function of the applied field for single-crystal diamond with $\vec{B}||\langle 100\rangle$. At this orientation the four $\langle 111\rangle$ axes are at $\theta=54.74°$. In the experiment, a slight splitting of the lines due to alignment errors of $\lesssim 2°$ was observed. Centers of the split lines are plotted. Curves are calculated with the parameters from Eq. (19).

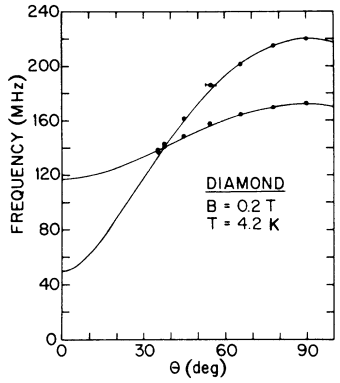

FIG. 6. Mu* precession frequencies as a function of the angle θ, the angle between the applied field, and the [111] symmetry axis. Curves are calculated with the parameters from Eq. (19).

formation probabilities for the muon states in this sample are included in Table III.

C. Temperature dependence of the Mu* hyperfine interaction

The temperature dependence of the anomalous muonium hyperfine constants in Si has been measured by Blazey *et al.*[5] With an increase in temperature from 4 to 150 K, a decrease of both $A_{||}$ and $A_{\perp}$ by about 1% was observed. This temperature dependence was attributed to the interaction of the paramagnetic Mu* center with host phonons. For an interaction with the long-wavelength part of a Debye phonon spectrum, the hyperfine interaction should vary as[8]

$$A(T)=A(0)\left[1-C\left[\frac{T}{\Theta_D}\right]^4\int_0^{\Theta_D/T}\frac{x^3}{e^x-1}dx\right], \tag{20}$$

where Θ_D is the Debye temperature and C is a coupling constant.

A second model of phonon interaction considers only coupling to a single-phonon mode with frequency ν and leads to the temperature dependence[9]

$$A(T)=A(0)\{1-C'[\coth(h\nu/kT)-1]\}\ . \tag{21}$$

Zero-field frequencies of anomalous muonium in diamond were measured with the powder sample in the temperature range 4.2 to 925 K, and the observed frequencies (Fig. 7) always satisfied the relation $\nu_1+\nu_2=\nu_3$. The hyperfine constants resulting from Eq. (13) are plotted in Fig. 8.

A fit of the data to the Debye model Eq. (20) yields the following parameters:

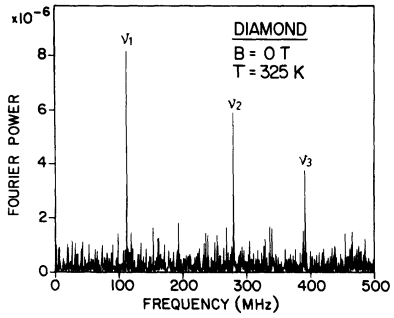

FIG. 7. Zero-field frequency spectrum of Mu* measured in diamond at 325 K. The lines ν_1, ν_2, and ν_3 are characteristic for Mu*.

$$
\begin{aligned}
&|A_\perp(0)|/h = 392.586 \pm 0.055 \text{ MHz}, \\
&|A_{||}(0)/h = 167.983 \pm 0.057 \text{ MHz}, \\
&C_\perp = 0.379 \pm 0.019, \\
&C_{||} = 0.727 \pm 0.036, \\
&\Theta_D = 1902 \pm 51 \text{ K}.
\end{aligned} \tag{22}
$$

The Debye temperature found compares well with the averaged calorimetric Debye temperature of diamond[10] ($\Theta_D = 1860$ K) in this temperature range.

The curves shown in Fig. 8 are calculated with Eq. (20) using the parameters given above. Within errors, $A_{||}(0)$ and $A_\perp(0)$ are equal to the values obtained from the single-crystal measurements [Eq. (19)].

A fit to the second model [Eq. (21)] results in the parameters

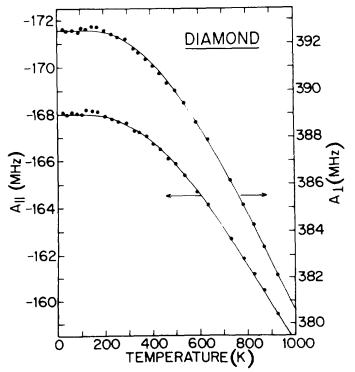

FIG. 8. Temperature dependence of $A_{||}$ and $A_\perp$ measured on the diamond powder sample. The lines fitted to the data points correspond to the Debye model [Eq. (20)].

$$
\begin{aligned}
&|A_\perp(0)|/h = 392.528 \pm 0.070 \text{ MHZ}, \\
&|A_{||}(0)|/h = 167.936 \pm 0.075 \text{ MHz}, \\
&C'_\perp = 0.0407 \pm 0.0021, \\
&C'_{||} = 0.0781 \pm 0.0041, \\
&\Theta = h\nu/k = 653 \pm 19 \text{ K}.
\end{aligned} \tag{23}
$$

The fit to this model results in a considerably inferior χ^2, and the fitted frequency

$$\nu = k\Theta/h = 1.36 \times 10^{13} \text{ Hz}$$

cannot be associated with any special feature in the phonon distribution.[10] Since the data are better described by Eq. (20) and since the obtained Debye temperature has the correct value, the Debye model seems preferable. Blazey *et al.*[5] argued that the monotonic decrease of their A values and the nonmonotonic variation of the thermal expansion of Si excludes the possibility that lattice dilation is the major cause of the temperature dependence of $A_\perp$ and $A_{||}$. Since the thermal expansion of diamond[11] is even smaller (but monotonic) than that of Si, we may conclude by analogy that also for diamond lattice dilation is not the major cause of the effect.

It is noteworthy that the coupling constants obtained for Si ($C_{||} = 0.5$, $C_\perp = 1.1$ for the Debye model in our notation) are similar in magnitude to those for diamond. Because of the limited temperature range where signals of Mu* in Si could be observed, the data of Blazey *et al.* did not allow a discrimination between the two models, nor was it possible to extract a value of Θ_D from the data.

D. Measurement on Mu* at the "magic" field

Since the Mu* Hamiltonian and the energy eigenvalues [Eqs. (3) and (9)] strongly depend on crystal orientation θ, in general, no μSR frequencies can be detected in a powder sample in an applied field. But as has been shown in Sec. II B, there exists a magic field B_M where the frequency ν_{12} is independent of θ and hence the magic frequency $\nu_M = \nu_{12}$ can be observed. The field dependence of the frequency ν_{12}, obtained by numerical diagonalization of H_{Mu^*} for various angles θ, is shown in Fig. 9. The lines cross to an extremely good approximation at one point.

Experimentally, the linewidth λ of the frequency ν_{12} is measured as a function of B near the estimated B_M, and a minimum occurs at B_M. Such

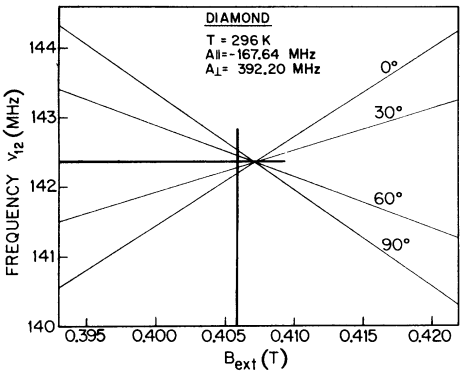

FIG. 9. Calculated frequencies ν_{12} for Mu* in diamond as a function of the external field B for various angles θ. The parameters used were obtained from zero-field measurements at 296 K, and $g_e = g_e(\text{vac})$ was assumed. Curves cross at the magic field $B_M = 0.407\,18$ T and the magic frequency $\nu_M = 142.36$ MHz. Measurement shown in Fig. 10 was done at the indicated field B_{ext} and gave the indicated frequency.

measurements are relatively fast and give precise values for the hyperfine constants without accurate sample orientation, but approximate starting values for $A_{||}$ and $A_{\perp}$ are required.

Using the parameters from the zero-field measurements (Fig. 8), it can be predicted [Eq. (11)] that

$$B_M = 0.4072 \text{ T}$$

and

$$\nu_M = 142.36 \text{ MHz}$$

at 296 K. A measurement at the slightly lower field $B = 0.4059$ T and at 296 K (Fig. 10) gave the results

$$\nu_M = 142.37 \pm 0.02 \text{ MHz}\,, \qquad \lambda = 0.25 \pm 0.10\ \mu\text{s}^{-1}\,. \tag{24}$$

This confirms the result of Sec. IV B that $A_{||}$ and $A_{\perp}$ have different signs, because in the opposite case B_M would be 1.0 T.

The accuracy with which the frequencies $\nu_{12}(\theta)$ cross at a point is a sensitive function of any anisotropy in the electronic Zeeman energy. This fact can be used to give an upper limit for the anisotropy. Comparing the damping rate λ of Eq. (24) with the expected frequency distribution at B_M for an anisotropic g_e factor in H_{Mu^*} [Eq. (3)], one obtains

$$|g_{\perp} - g_{||}| \leq 0.02\,, \tag{25}$$

where $g_{\perp}$ and $g_{||}$ also refer to the $\langle 111 \rangle$ axis.

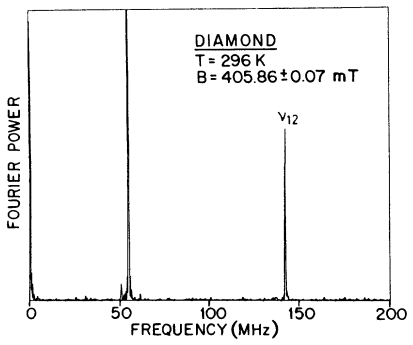

FIG. 10. Frequency spectrum of Mu* in the diamond powder sample near the magic field B_M. Magic frequency ν_{12} is observed. Line at 55.01 MHz corresponds to the Larmor precession of muons stopped in the sample container.

E. Formation of Mu* at high temperatures

The investigation of Mu* in the powder sample in zero field showed the following two unexpected phenomena (Figs. 7, 11, and 12):

(i) a strong increase of the precession amplitudes with temperature, and

(ii) a variation of the relative amplitudes of the three lines. The expected amplitude ratio for lines ν_1, ν_2, and ν_3 should be 2:2:1, as given by Eq. (14).

These two phenomena shed light on the process of Mu* formation in diamond. Assuming that there exists a short lived and hence unobserved precursor state to Mu*, the observed zero-field polarization of Mu* is changed from that given in Eq. (14) and

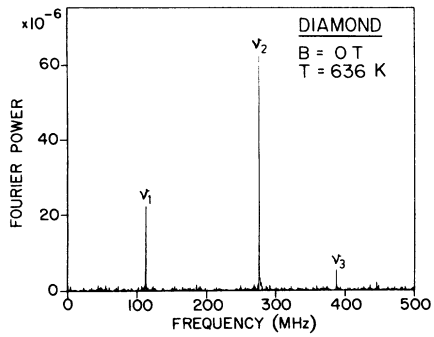

FIG. 11. Zero-field frequency spectrum of Mu* measured in diamond at 636 K.

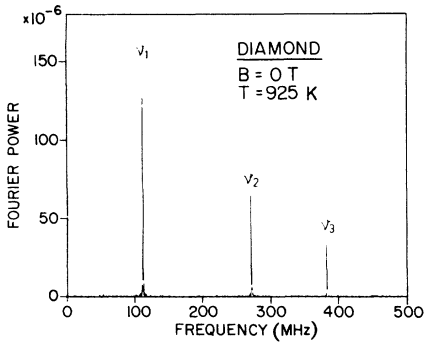

FIG. 12. Frequency spectrum for diamond measured at 925 K in zero external field.

may be written in the form

$$P_x(t)=\tfrac{1}{6}[1+2a_1\cos(\omega_1 t+\phi_1)+2a_2\cos(\omega_2 t+\phi_2)+a_3\cos(\omega_3 t+\phi_3)]P_x(0)\ , \tag{26}$$

where the amplitudes a_j $(j=1,2,3)$ and phases ϕ_j depend on the state of the muon prior to its incorporation in Mu* and on the transition rate from this state to Mu*. The measured precession amplitudes (not normalized) are plotted in Fig. 13. The constant values for $T<400$ K can be explained by almost instantaneous Mu* formation for a particular fraction of the incoming muons. In this case

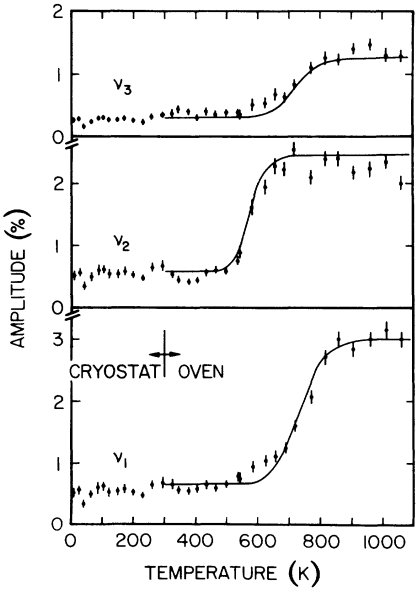

FIG. 13. Measured precession amplitudes (not normalized) of the zero-field Mu* lines ν_1, ν_2, and ν_3 as a function of temperature. The curves correspond to the fit discussed in the text.

one has

$$a_1=a_2=a_3=1$$

and

$$\phi_1=\phi_2=\phi_3=0\ .$$

Normal muonium was observed below 150 K in a transverse field with a hyperfine frequency $\omega_0=2\pi(3711)$ MHz (see Sec. IV A). If this muonium state disappears with increasing temperature because of transformation into Mu*, the amplitudes and phases of the three zero-field frequencies will depend strongly on the Mu→Mu* reaction rate Λ.

The general theory of spin-polarization transfer in transitions among muon states will be discussed elsewhere.[12] Here, the results pertinent to the zero-field experiments are given. Assuming that the electron polarization is conserved in the reaction Mu→Mu*, one obtains

$$\begin{aligned}
a_1&=1/[1+(\omega_0-\omega_1)^2/\Lambda^2]^{1/2}\ ,\\
a_2&=1/(1+\omega_2^2/\Lambda^2)^{1/2}\ ,\\
a_3&=1/[1+(\omega_0-\omega_3)^2/\Lambda^2]^{1/2}\ ,\\
\phi_1&=\arctan[(\omega_0-\omega_1)/\Lambda]\ ,\\
\phi_2&=\arctan(\omega_2/\Lambda)\ ,\\
\phi_3&=\arctan[(\omega_0-\omega_3)/\Lambda]\ .
\end{aligned} \tag{27}$$

Since ω_0 is one order of magnitude larger than ω_j, the amplitude a_2 shows a Λ dependence distinctly different from a_1 and a_3, as shown in Fig. 14.

One obtains quite different results if the electron spin polarization is not conserved in the reaction

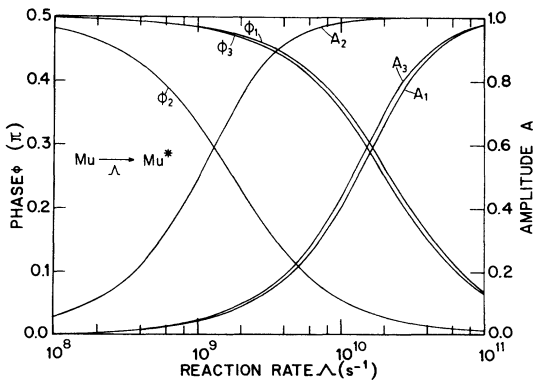

FIG. 14. Amplitudes and phases of the three Mu* lines in zero field as a function of the reaction rate Λ for the transformation Mu→Mu*. Notice that A_2 at intermediate Λ is much stronger than lines 1 and 2.

Mu→Mu*:

$$-2a_j \sin\phi_j = \frac{\omega_j/\Lambda'}{1+\omega_j^2/\Lambda'^2} - \frac{1}{2}\frac{(\omega_0-\omega_j)/\Lambda'}{1+(\omega_0-\omega_j)^2/\Lambda'^2} + \frac{1}{2}\frac{(\omega_0+\omega_j)/\Lambda'}{1+(\omega_0+\omega_j)^2/\Lambda'^2} , \quad (28)$$

$$2a_j \cos\phi_j = \frac{1}{1+\omega_j^2/\Lambda'^2} + \frac{1}{2}\frac{1}{1+(\omega_0-\omega_j)^2/\Lambda'^2} + \frac{1}{2}\frac{1}{1+(\omega_0+\omega_j)^2/\Lambda'^2} .$$

In contrast to the case where the electron polarization is conserved, there is no dramatic difference in the amplitudes for a given value of Λ', and one always has the sequence $a_1 \geq a_2 \geq a_3$ as shown in Fig. 15.

For the case where Mu* is formed directly from a "naked" μ^+ with reaction rate Λ', Eqs. (28) reduce to

$$a_j = 1/(1+\omega_j^2/\Lambda'^2)^{1/2} , \quad \phi_j = \arctan(\omega_j/\Lambda') . \quad (29)$$

Equations (27), (28), and (29) apply to the case where a single transformation (Mu→Mu* or μ^+→Mu*) occurs. Each type i of transformation involves not only a Λ-dependent amplitude a_j^i for each Mu* line, but also a Λ-dependent initial phase angle ϕ_j^i. If both transformations occur simultaneously, the resulting amplitudes and phases are given by

$$a_j \sin\phi_j = \sum_{i=1}^{2} a_j^i \sin\phi_j^i , \quad a_j \cos\phi_j = \sum_{i=1}^{2} a_j^i \cos\phi_j^i . \quad (30)$$

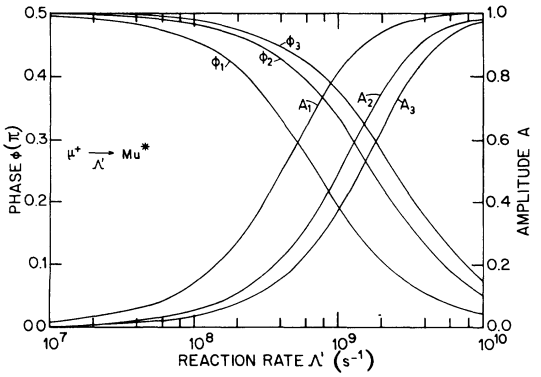

FIG. 15. Amplitudes of the zero-field Mu* lines ν_1, ν_2, and ν_3 as a function of the reaction rate Λ' for the transformation μ^+→Mu*.

The observed variation of the amplitudes with temperature can now be discussed in terms of these theoretical results. The high-temperature data (see Fig. 13) show a dramatic increase of the amplitude a_2 at 600 K accompanied by a slight increase of a_1 and a_3. This distinctive behavior of the intermediate frequency line is strong evidence for the formation of Mu* from Mu with the conservation of both muon and electron polarization.

The problem of the conservation of electron polarization during reactions of muonium has been discussed extensively.[13] Conservation of polarization is generally assumed in current theories of radical termination reactions and has been demonstrated in several ESR experiments. In μSR chemistry, the precession frequencies obtained with tetramethylethylene in zero field[14] have been interpreted with muonium as radical percursor and assuming spin conservation during the reaction.

An attempt was made to fit the data to this Mu→Mu* reaction model under the assumption that at low temperature 10% of the incoming μ^+ form Mu* instantaneously (see Table III). It was further assumed that the reaction rate is given by

$$\Lambda = \psi \exp(-U/kT) .$$

The fit indicated in Fig. 13 corresponds to values for the reaction Mu→Mu*:

$$U/k = 7000 \text{ K} , \quad \psi = 4\times10^{14} \text{ s}^{-1} . \quad (31)$$

This temperature dependence for Λ is not compatible with the measured Mu relaxation rate (Table II). The latter is describable using quite different values: $U/k = 500$ K and $\psi = 10^8$ s^{-1}. The discrepancies suggest that an additional process such as a temperature-dependent relaxation of the muonium electron spin is responsible for the disappearance of the Mu signals.

V. ELECTRONIC STRUCTURE OF Mu AND Mu*

Table IV lists the hyperfine coupling constants of Mu and Mu* in diamond together with the corresponding values obtained for the isostructural materials silicon and germanium. A point to be noted is that, although diamond has the smallest lattice constant of the three elements, its coupling constants for Mu and Mu* are largest and hence most vacuumlike.

TABLE IV. Comparison of the hyperfine coupling constants of Mu and Mu* at 0 K.

	Mu		Mu*	
	A/h (MHz)	$f=A/A_{vac}$	$A_{\|\|}/h$ (MHz)	$A_{\perp}/h$ (MHz)
Diamond	3711	0.831	−167.9	392.5
Silicon	2012	0.450	16.8	92.6
Germanium	2361	0.529	26.8	130.7
Vacuum	4463	1.000		

Shallow donors and acceptors in semiconductors are well described by the effective mass theory.[15] Deep levels whose bound-state orbits are comparable to the interatomic spacing, on the other hand, are more difficult to treat. Hydrogen and its "isotope" muonium are the simplest examples of interstitial donor impurities, and their microscopic description has been the subject of several theoretical investigations.[16–23]

Wang and Kittel[16] studied muonium in Si and Ge using phenomenological models. They obtained reasonable values for the hyperfine constants both in a cavity model and in a model using a space-dependent dielectric function, provided that the electron mass was taken as the free-electron mass. The latter assumption, however, cannot be justified in the framework of the effective-mass theory as has been discussed by Pantelides.[20]

Recent theories[22,23] which take into account the intervalley mixing effect on donor impurities in many-valley semiconductors lead to a deep ground-state level for a hydrogen impurity. Whereas in Ref. 22 this deep state is predicted to occur only for an interstitial impurity, the intervalley interference effect considered in Ref. 23 should cause a deep level for both interstitial and substitutional sites. In both theories the effective-mass approach is extended to account for many-valley contributions. For a point-charge impurity, the ground-state binding energy then becomes larger than the fundamental gap, indicating that the effective-mass approach breaks down. This breakdown is attributed to the formation of a deep level. Thus the prediction of the deep donor character of hydrogen and muonium is only a qualitative one, and extended effective-mass theories are inherently inadequate to quantitatively describe deep states.

The new data on muonium in diamond have led us to the investigation of the question whether the models introduced by Wang and Kittel[16] (the so-called "cavity model" and the "dielectric function approach") also work in the case of normal muonium in diamond. These phenomenological models, although admittedly crude, are at present the only ones which lead to quantitative statements.

In the cavity model, the potential is assumed to be given by

$$V(r)=\begin{cases}\dfrac{-e^2}{4\pi\epsilon_0}\left[\dfrac{1}{r}-\dfrac{1}{R}+\dfrac{1}{\epsilon R}\right] & \text{for } r\le R\ ,\\ \dfrac{-e^2}{4\pi\epsilon_0}\left[\dfrac{1}{\epsilon r}\right] & \text{for } r\ge R\ ,\end{cases} \tag{32}$$

where ϵ is the static dielectric constant and ϵ_0 the permitivity of vacuum. The potential is continuous at the cavity radius R. There are two probable symmetrical interstitial sites for muonium in the diamond structure; one with tetrahedral local symmetry and one with hexagonal local symmetry.[24] If the corresponding cavity radii R_T and R_H are determined from the radius of the interstitial sphere that fits inside the touching hard spheres of the lattice atoms, one obtains $R_T=0.227a$ and $R_H=0.198a$, where a is the lattice constant. The values for R_T and R_H are given in Table V. The ground-state energies for C, Si, and Ge of the potential (32) are shown in Table VI. The enhance-

TABLE V. Parameter values for diamond, silicon, and germanium. R_T and R_H are the cavity radii for the touching spheres model for the tetrahedral and hexagonal interstitial sites. Q is the inverse screening length for the dielectric function, ϵ is the static dielectric constant, a the lattice constant, and a_0 the Bohr radius ($a_0=0.53$ Å).

	a (Å)	ϵ	R_T (a_0)	R_H (a_0)	Q (a_0^{-1})
C	3.56	5.7	1.45	1.33	1.15
Si	5.43	11.9	2.22	2.03	0.92
Ge	5.65	16.0	2.31	2.12	0.82

TABLE VI. Results obtained for Mu in diamond, silicon, and germanium for different models. The potentials refer to the corresponding equations in the text. The ground-state energies E are in Rydberg units (1 Ry $=13.6$ eV). The sequence of the calculated enhancement factors $f=A/A_{\text{vac}}$ should be compared with the experimental results. T stands for tetrahedral site and H for hexagonal site.

Potential	Eq. (32) T		Eq. (32) H		Eq. (35)		Eq. (36)		Experiment
	E	f	E	f	E	f	E	f	f
C	−0.108	0.419	−0.086	0.313	−0.151	0.381	−0.054	0.114	0.829
Si	−0.220	0.834	−0.168	0.754	−0.115	0.428	−0.033	0.170	0.450
Ge	−0.226	0.856	−0.174	0.786	−0.129	0.487	−0.028	0.175	0.529
Sequence	$f_C<f_{Si}<f_{Ge}$		$f_C<f_{Si}<f_{Ge}$		$f_C<f_{Si}<f_{Ge}$		$f_C<f_{Si}<f_{Ge}$		$f_C>f_{Ge}>f_{Si}$

ment factor f is defined by

$$f\equiv|\psi(0)|^2/|\psi_{\text{vac}}(0)|^2\,, \tag{33}$$

where

$$|\psi_{\text{vac}}(0)|^2=(\pi a_0^3)^{-1}\,.$$

Although the actual cavity radius could be somewhat different from R_T or R_H, it is evident that the cavity model always leads to $f_C<f_{Si}<f_{Ge}$ in contrast to the experimental results.

The dielectric function approach of Wang and Kittel assumes a potential of the form

$$V(r)=-\frac{e^2}{4\pi\epsilon_0\epsilon(r)r}\,, \tag{34}$$

where the space-dependent dielectric function $\epsilon(r)$ is obtained as the Fourier transform of $\epsilon(q)$, which can be calculated from the band structure. In Ref. 16 the model dielectric function

$$\epsilon(q)=\epsilon\frac{q^2+Q^2}{\epsilon q^2+Q^2} \tag{35}$$

proposed by Hermanson[25] was used with the screening parameter Q determined by fitting Eq. (35) to the spherically averaged calculated[26] values of $\epsilon(\vec{q})$. The corresponding values for Q used in the present calculation are given in Table V.

Another model for $\epsilon(r)$ was proposed by Resta[27] who, by solving the linearized Thomas-Fermi equation, obtained the following form:

$$\epsilon(r)=\begin{cases}\epsilon\kappa R\{\sinh[\kappa(R-r)+\kappa r]\}^{-1} & \text{for } r\le R\,,\\ \epsilon & \text{for } r\ge R\,,\end{cases} \tag{36}$$

where $\kappa\equiv(4k_F/\pi)^{1/2}$ and $R=2.76$, 4.28, and $4.71a_0$ for C, Si, and Ge. The f values obtained for the dielectric function (36) are generally even lower than those obtained from (35).

The results for all these models are summarized in Table VI. All models lead to deep bound states, which is a consequence of the use of the bare electron mass, but they predict the wrong sequence for the enhancement factor. The models with a factor f close to the data for Si and Ge give an f_C value lower than f_{Si} or f_{Ge}, in contrast to the measurements.

From these results it is concluded that the apparent quantitative success of the models of Wang and Kittel for muonium in Si and Ge does not hold in the case of diamond. Further calculations are needed which take account of the detailed electronic structure of the host.

Recently, a self-consistent pseudopotential method has been used[21] to treat the hydrogen interstitial impurity in germanium. By including strong intra-atomic correlation effects, it was found that a singly occupied H-1s deep donor state exists which lies at least 1 eV and perhaps as much as 6 eV below the Ge-valence-band maximum. To decide whether this deep donor state is the one seen in μSR experiments, one should have similar calculations for silicon and diamond.

The electronic structure of the anomalous muonium state has so far not been investigated by microscopic calculations. The phenomenological models which have been proposed are reviewed by Estle.[28] The obvious difficulty in explaining the two different muonium states are the unknown sites of Mu and Mu*.

VI. SUMMARY AND CONCLUSIONS

The data presented in this article clearly establish the existence of two different muonium states in diamond. The basic features of these two states agree with those observed in Si (Ref. 2) and Ge.[3] The normal muonium state (Mu) is described by an isotropic spin Hamiltonian with a hyperfine fre-

quency reduced from the vacuum value. The anomalous muonium state (Mu*) is described by an axially symmetric spin Hamiltonian with the symmetry axis parallel to one of the four ⟨111⟩ axes. The hyperfine coupling constants are of the same order of magnitude as those for Si and Ge (see Table IV).

Differences in the behavior of the muonium states in diamond as compared to Si and Ge are apparent in the temperature dependence of the formation probabilities and relaxation rates. In Si and Ge the relaxation rates λ of both Mu and Mu* increase with increasing temperatures and the signals disappear ($\lambda \gtrsim 10\ \mu s^{-1}$) at about 200 K (300 K) for Mu* (Mu) in Si and at 80 K (100 K) in Ge. This relaxation is usually attributed to the scattering of phonons or charge carriers by the muonium atom, resulting in a spin flip of the bound electron. If at higher temperatures the rate of spin flipping exceeds the hyperfine frequency, a signal with the bare μ^+ frequency should be observed. This effect has been verified both in Si (Ref. 29) and Ge.[30]

In C, on the other hand, the situation is quite different. Mu disappears around 150 K, whereas the Mu* signals show constant relaxation rates and increasing amplitudes at higher temperatures. This indicates that Mu* in diamond has a lower total energy than Mu, whereas the situation may be reversed in Si and Ge. The stability of Mu* in diamond is also indicated by the observed increase of the Mu* amplitudes at about 600 K which can be explained by Mu→Mu* transitions, as has been discussed in Sec. IV E. Analogous transitions of Mu*→Mu in Si and Ge have not been reported. This may be due to the relaxation of the bound electrons mentioned above which destroys the hyperfine structure of the paramagnetic states. In diamond, these relaxation processes are not effective since there are no free charge carriers and since Raman processes are suppressed at the relevant temperatures due to the high Debye temperature. In Si and Ge a similar transition should, however, be indirectly observable since it influences the behavior of the amplitude and phase of the μ^+ signal as a function of temperature and transverse field as well as the dependence of the polarization on an applied longitudinal field. In this respect it should be noted that measurements of the μ^+ signal in Ge at around 200 K showed a temperature- and field-dependent phase shift.[30] This was interpreted by the authors as an indication of a chemical reaction or thermal ionization of Mu. The present results for diamond makes it seem plausible that this observation in Ge could be reinterpreted as being due to a transition between normal and anomalous muonium.

Another question which must be addressed is the possible influence of impurities on the formation of Mu or Mu*. Despite recent experiments[31] which seem to indicate that the Mu state in Ge is related to C impurities, we believe that the formation of Mu and Mu* is an intrinsic property of group-IV semiconductors for the following reasons: (i) The formation probabilities in the two diamond samples used in the present experiment are equal (see Table III) although the impurity contents differ markedly. (ii) The direct observation[6] of the Mu hyperfine transition in zero field in high-purity Si and Ge shows that Mu is formed in a time less than 10^{-10} s after the μ^+ enters the target. There is insufficient time for a muon to reach an impurity and become trapped at low temperature. (iii) A recent experiment[32] showed no difference in muonium formation in ultrapure Ge crystals grown under quite different conditions. (iv) The observations of Mu and Mu* with similar properties in Si, Ge, and diamond make the assumption of any defect-related formation very unlikely.

The electronic structure of neither Mu nor Mu* is understood. The models of Wang and Kittel,[16] which gave a reasonable explanation for Mu in Si and Ge, fail for C. No quantitative model for Mu* exists so far. Such a model should account for the observed hyperfine parameters in all three elements. The suggestion that the two muonium states may be identified with muonium atoms at the tetrahedral and hexagonal interstitial sites is plausible but lacks any experimental or theoretical evidence. The variation of the hyperfine constants of Mu* with temperature is accurately accounted for by a Debye model and is similar to that observed in Si.

In conclusion, we hope that the data which are now available for the muonium states in Si, Ge, and diamond will stimulate more theoretical work on this particularly simple example of an interstitial impurity in semiconductors. The major experimental challenge is the identification of the sites of Mu and Mu*.

ACKNOWLEDGMENTS

Acknowledgment is made to Professor J. P. Blaser, Director of SIN, for his support and interest in this research project. Particular appreciа-

tion must be given to Dr. H. B. Dyer of Mines de Beers Industrial Diamonds (Pty) Ltd., for his kindness and scientific interest in both finding a large diamond of such excellent quality and for arranging the loan thereof for this work. We are grateful to P. Baltensperger, Jewelers & Cie. Zürich for their kind assistance. We acknowledge the theoretical contributions of S. Estreicher and the help with the data analysis by M. Richner, both of the University of Zurich. Two of the authors (J.P.F.S. and M.C.S.) acknowledge the support from the University of the Witwatersrand. This work was supported by SIN and the Swiss National Science Foundation.

[1]J. H. Brewer, K. M. Crowe, F. N. Gygax, R. F. Johnson, B. D. Patterson, D. G. Fleming, and A. Schenck, Phys. Rev. Lett. 31, 143 (1973).
[2]B. D. Patterson, A. Hintermann, W. Kündig, P. F. Meier, F. Waldner, H. Graf, E. Recknagel, A. Weidinger, and T. Wichert, Phys. Rev. Lett. 40, 1347 (1978).
[3]E. Holzschuh, H. Graf, E. Recknagel, A. Weidinger, T. Wichert, and P. F. Meier, Phys. Rev. B 20, 4391 (1979).
[4]A. B. Denison, H. Graf, W. Kündig, and P. F. Meier, Helv. Phys. Acta 52, 460 (1979).
[5]K. W. Blazey, J. A. Brown, D. W. Cooke, S. A. Dodds, T. L. Estle, R. H. Heffner, M. Leon, and D. A. Vanderwater, Hyperfine Interact. 8, 381 (1981).
[6]E. Holzschuh, W. Kündig, and B. D. Patterson, Hyperfine Interact. 8, 819 (1981), and (unpublished).
[7]A. Hintermann, P. F. Meier, and B. D. Patterson, Am. J. Phys. 48, 956 (1980).
[8]E. Simanek and R. Orbach, Phys. Rev. 145, 191 (1966).
[9]W. Dreybrodt, Phys. Status Solidi 21, 99 (1967).
[10]G. Dolling and R. A. Cowley, Proc. Phys. Soc. 88, 463 (1966).
[11]S. I. Novikova, Fiz. Tverd. Tela (Leningrad) 2, 43 (1960) [Sov. Phys.—Solid State 2, 37 (1960)].
[12]P. F. Meier, Phys. Rev. A 25, 1287 (1982).
[13]P. Percival and H. Fischer, Chem. Phys. 16, 89 (1976).
[14]E. Roduner and H. Fischer, Chem. Phys. 54, 261 (1981).
[15]W. Kohn, in *Solid State Physics,* edited by F. Seitz and D. Turnbell (Academic, New York, 1957), Vol. V.
[16]J. S. Wang and C. Kittel, Phys. Rev. B 7, 713 (1973).
[17]V. A. Singh, C. Weigel, J. W. Corbett, and L. M. Roth, Phys. Status Solidi 81, 637 (1977).
[18]A. Coker, T. Lee, and T. P. Das, Hyperfine Interact. 4, 821 (1978).
[19]C. O. Rodriguez, M. Jaros, and S. Brand, Solid State Commun. 31, 43 (1979).
[20]S. T. Pantelides, Hyperfine Interact. 6, 145 (1979).
[21]W. E. Pickett, M. L. Cohen, and C. Kittel, Phys. Rev. B 20, 5050 (1979).
[22]M. Altarelli and W. Y. Hsu, Phys. Rev. Lett. 43, 1346 (1979).
[23]L. Resca and R. Resta, Phys. Rev. Lett. 44, 1340 (1980).
[24]K. Weiser, Phys. Rev. 126, 1427 (1962).
[25]J. Hermanson, Phys. Rev. 150, 660 (1966).
[26]P. K. W. Vinsome and D. Richardson, J. Phys. C 4, 2650 (1971).
[27]R. Resta, Phys. Rev. B 16, 2717 (1977).
[28]T. L. Estle, Hyperfine Interact. 8, 365 (1981).
[29]S. G. Barsov *et al.*, Zh. Eksp. Teor. Fiz. 76, 2198 (1979) [Sov. Phys.—JETP 49, 1110 (1979)].
[30]V. I. Kudinov *et al.*, Zh. Eksp. Teor. Fiz. 70, 2041 (1976) [Sov. Phys.—JETP 43, 1065 (1976)].
[31]E. E. Haller, A. Seeger (private communication).
[32]C. W. Clawson, E. E. Haller, K. M. Crowe, S. S. Rosenblum, and J. H. Brewer, Hyperfine Interact. 8, 417 (1981).